2010 SCEC Annual Report

Project 119941

Integrating earthquake surface deformation and seismicity in a 3-dimensional analysis of multi-fault rupture mechanics

David D. Pollard and Betsy Madden

Dept. of Geological & Environmental Sciences, Stanford University, Stanford, CA 94305

The critical role of fault structure in the earthquake rupture process (Harris, 2004) underscores the importance of characterizing the complex structure of faults involved in the 1992 Landers earthquake in three-dimensions (3D). As proposed in our 2010 application for SCEC funding, we constrain fault structure by comparing recorded model right-lateral surface slip and inferred focal mechanisms with model failure planes at the locations of large aftershocks. This approach allows for evaluation of fault geometries that produce similar slip distributions, in regions of complex surface rupture, and where faults do not break the surface. The refined structure of major faults at Landers includes a shallow vertical termination of the western fault located at the southern tip of the Johnson Valley Fault (JVF) and extension south of the eastern fault below the surface. The central JVF dips 80°W and the gap in right-lateral slip along the Homestead Valley Fault (HVF) is best explained by a 80°W dip, rather than by a fault discontinuity or bend. Small fault discontinuities near the surface may control deficits in right-lateral surface slip. Results suggest that focal mechanism orientations may be dominated by the local stress field from main shock fault slip and sensitive to fault geometry. Comparison of these focal mechanisms with model failure planes provides a mechanical basis for discriminating between the two aftershock nodal planes. We observe that slip along non-planar faults, even with friction of 0.6, contributes to failure planes in a variety of orientations at different locations, which do not necessarily reflect the orientation of the main shock faults or the sense of slip along those faults.

Introduction

We integrate high quality geological surface offset data and seismological aftershock data from the Landers earthquake to constrain fault structure of the M7.3 Landers earthquake, which ruptured segments of five sub-parallel, northwest-southeast striking faults in the Eastern California Shear Zone in the Mojave Desert of California including the Johnson Valley Fault (JVF), Homestead Valley Fault (HVF), Landers-Kickapoo Fault (LKF), and Emerson Fault (EF). Our focus is on the JVF, LKF and southern HVF due to the large fluctuations of lateral slip between 300cm and 100cm along the northern HVF and the sparse slip measurements along the entire EF. Fault geometries are compared in three areas of interest where distinctive surface rupture patterns and large, early aftershocks with low focal mechanism uncertainty suggest that important insights can be obtained about the subsurface structure. These areas are as follows: 1) the southern tip of the JVF, where slip is distributed across two main shock faults; 2) the Flamingo Heights region along the central JVF, where right-lateral slip decreases from greater than 200cm to less than 100cm and is distributed across one major and multiple minor main shock faults; and 3) the ‘slip gap’ along the HVF, where the rupture crosses an outcrop of quartz monzonite north of the JVF-HVF stepover and right-lateral offset decreases to zero (Spotila and Sieh, 1995).

Data & Methods

We compare model and observed dextral surface offset to constrain fault geometries. The surface rupture data utilized are the combined work of many geologists, compiled and digitized by the California Geological Survey (CGS) (Bryant, 1992, 1994, 2004; CGS, 2002). Structural models contain only one main fault where, in many locations, multiple faults are observed. For comparison with model slip, cumulative observed slip values were determined by summing right-lateral offset measurements across sub-parallel, overlapping main shock faults.

Aftershocks are utilized to provide additional constraint on fault models, following the hypothesis that they reflect the local stress state dominated by the geometry of the major faults that slip during the main shock. Aftershock relocations are by Zanzerkia (2003) and focal mechanisms were determined with the software program HASH (Hardebeck and Shearer, 2002). Events occurring more than six months after the main shock, events smaller than M3, and events with fault plane uncertainties greater than 35° are excluded. In each area of interest, we select the four largest, earliest aftershock focal mechanisms. At each aftershock location, the two Coulomb failure planes (Anderson, 1942; Pollard and Fletcher, 2005) are determined from the model stress tensor resulting from slip along model faults.

Both aftershock nodal planes and model failure planes are included in analyses. The first model failure plane is compared to the first and second aftershock fault plane solution and the second model failure plane is compared to the first and second aftershock fault plane solution. We report the set of two pairs of failure planes for each aftershock that minimize 'diffFP' and 'diffR', the parameters used to quantify the difference between aftershock and model planes. DiffFP is smaller of the two angles formed by the downward pointing normal vector to the aftershock fault plane and the downward or upward pointing normal vector to the model failure plane. 'DiffR' is the angle between the aftershock and model unit slip vectors. 'Good fit' failure planes are those with both diffFP and diffR within the fault plane uncertainty of the fault plane solution. A 'best-fit' model failure plane is the failure plane within uncertainty that most closely matches the aftershock fault plane. In some locations, several models produce failure planes with similar diffFP and diffR and all are referred to as best-fits. A preferred model is constructed from the model geometries that produce the best-fit failure planes.

Three-Dimensional Structural Models

We compare results from models with major main shock fault geometries that differ in dip and continuity in the three areas of interest, referred to as the 'alternative models', with one another and with a model constructed from the Community Fault Model (CFM) (Plesch et al, 2002), as shown in Figure 1. The alternative model faults were built in gOcad from the digitized traces of the major main shock faults from CGS (2002) and Bryant (2004) and altering the dip and continuity of the JVF, LKF and HVF in the areas of interest. The CFM is vertical and continuous from the southern tip of the JVF, through the LKF, to the northern end of the HVF. 10km was selected for the fault height because 97% of aftershocks occur above this depth. The height of the CFM is reduced from 15km to 10km for comparison.

All alternative models are continuous from the JVF to the LKF, but discontinuous from the LKF to the HVF. Model 1 (M1) includes three variations through the Flamingo Heights region: M1a dips 85°W, M1b dips 85°E, and M1c dips 80°W. All three models include both main shock faults at the southern tip of the JVF. Model 2 (M2) incorporates a vertical and discontinuous JVF through Flamingo Heights and only the western main shock fault at the southern tip of the JVF. The HVF in M1a-c and M2 is vertical and continuous, following the mapped trace through the slip gap. Models 3 (M3) and 4 (M4) are as in M1a along the JVF and LKF. Along the HVF, M3 follows the mapped fault trace in the slip gap at the surface, but is straight at depth, creating a dip of 80°W. M4 includes a discontinuous HVF through the slip gap.

Models are run in Poly3d, a quasi-static, linear elastic, boundary element program (Thomas, 1993; Maerten et al, 2005) from IGEOSS that admits non-planar 3D fault surfaces and irregular tiplines by discretizing surfaces into triangular dislocation elements. Poly3D relates traction or displacement discontinuity boundary conditions on dislocation elements and remote stress or strain conditions to displacement discontinuity along faults and stress, strain and displacement fields in the surrounding linear-elastic half-space (Comninou and Dunders, 1975; Thomas, 1993; Maerten et al, 2005). Homogeneous and isotropic elastic properties, remote stress magnitudes (compression positive), and remote stress orientations are consistent across all models. In combination with friction of 0.6, vertical gradients in the maximum and minimum horizontal stresses of 33MPa/km and 6MPa/km and a vertical gradient in the vertical stress of 30MPa/km produce slip on the JVF and HVF similar to that observed. The orientation of the maximum remote compressive stress is 011°, as the relative slip along the JVF and HVF are closest to the observed for this angle.

Evaluation of Fault Structure

Area of Interest 1: Southern Tip of the JVF

Normalized right-lateral slip distributions along the JVF and HVF for the CFM and the alternative models are shown in Figure 2 and a complete list of focal mechanisms, uncertainties, and model failure planes is given in Table 1. The faults at the southern tip of the JVF are too short to produce an informative slip distribution, but the aftershocks provide insight into model performance. All models except for the CFM produce good fit failure planes at #3079557 and #3037136. This suggests that near the surface, fault structure differs from the CFM, which lacks the eastern main shock fault and extends farther south along the western main shock fault than the alternative models. All models produce vertical, strike slip failure planes at #3032709 that strike ~30° to the direction of the remote maximum compressive stress, far from the orientation of the fault plane. Thus, the JVF may extend farther south at depth and perturb the local stress field here. At #3041147, the CFM, which lacks the western fault, produces the failure plane closest to the focal mechanism, though it is outside of uncertainty. The western fault at the tip of the JVF may not extend to the aftershock's depth (6.83km), as in the alternative models.

Area of Interest 2: Flamingo Heights Region along the Central JVF

The 80°W dipping JVF (M1c) and the discontinuous JVF (M2) both produce slip deficits near the observed slip deficit in the Flamingo Heights region at 3790km UTM Northing. M2 overshoots the observed normalized slip deficit of 0.2, sending slip to zero in the gap between its two fault segments, while M1c causes only a slight decrease in slip to a normalized offset of 0.7. The other models do not perform as well. The CFM produces the best-fit failure plane at #3085547, though all models produce good fit planes. No model produces a good fit plane at #3041761, located west of the major main shock fault and near numerous minor faults. M1c produces the best-fit failure planes at two locations, as well as a good fit plane in a third location, and best captures the local stress field. M2 fails to produce good fit planes in three of the four locations. Results support a dipping JVF through the region. That the observed slip deficit is greater than that produced by M1c suggests that the fault may have a dip lower than 80°W.

Area of Interest 3: HVF Slip Gap

Through the slip gap along the HVF, the straight and vertical CFM fails to produce a slip deficit similar to the observed, while the bent (M1a), dipping (M3) and discontinuous (M4) HVF geometries all produce slip minima. South of the slip gap, offset is best matched by offset along the southern segment of M4, yet the slip maximum along M4's northern segment is too far north. M1a and M2 produce greater normalized right-lateral slip along the HVF south of the slip gap than is observed, but produce slip distributions north of the slip gap similar to the observed. The

HVF has geometric complexity beyond that included in the CFM, but deciphering a best-fit geometry from the alternative models is difficult. Within and to the northeast of the quartz-monzonite outcrop, the CFM also fails to reproduce the local stress state. M3 does best at #3052180 and #3032488, providing evidence for a dipping HVF through the slip gap. The CFM does produce the best-fit failure to the east of the mapped thrust trace, suggesting that the HVF may remain vertical farther north into the quartz-monzonite outcrop, rather than following the mapped surface trace of the thrust fault, as do M1a, M3 and M4. Despite differences in model geometry at #3071282, all models produce similar, good fit right-lateral planes at this location.

Preferred Model Synthesis

The preferred model is built from the geometries that produce the best-fit right-lateral slip distributions and failure planes in the three areas of interest. It includes a bifurcated southern tip of the JVF with the western main shock fault extending from the surface to 2km depth and the eastern main shock fault extending 2.5km farther south at 10km depth. The central JVF is as in M1c, but dips 75°W, and the HVF is as in M3, but remains vertical farther north. The preferred model performs better than any of the original models. Its slip distribution captures some of the complexity of the observed slip distribution, with a larger slip deficit than M1c in the Flamingo Heights region and no right-lateral slip in the slip gap. The failure planes produced by the preferred model are good fits to seven of the twelve analyzed focal mechanisms. Two additional failure planes are improvements over the originals, but are outside of uncertainty.

An additional model tests the possibility that the slip deficits along the JVF and HVF are best reproduced by faults with high dips (JVF: 85°W, HVF: 80°W), but with local discontinuities in upper 2km of the surface. The model produces a very nice fit to the JVF and HVF slip distributions. The preferred model produces better fitting failure planes along the central JVF, however and while this additional model produces good fit planes through the slip gap, it does not perform as well as the preferred model in three of the four locations. It performs better in one location, however, near the southern extent of the discontinuity. Thus small, near-surface discontinuities of ~1-2km in height and 1-3km in length can produce the slip deficits observed, but failure plane are sensitive to the precise locations of such local discontinuities.

Discussion & Conclusions

The local stress field from slip along major faults is sensitive to differences in fault geometry, such as variations in fault dip, strike and continuity. Model Coulomb failure planes have a variety of orientations due to this heterogeneous stress field, even with friction of 0.6, and in many locations, the stress state inferred from a focal mechanism can be best reproduced by a particular fault geometry. This method allows for determination of the fault plane from the two provided in the focal mechanism without assuming that orientation of or slip on the aftershock fault planes matches the orientation of or slip on the major main shock faults.

In certain locations, models with different geometry produce similar failure planes. For example, the geometric differences of dip, strike and continuity incorporated into the three alternative models along the HVF (M1a, M3, M4) have similar effects on fault slip and produced similar failure planes at the locations of the four analyzed events. This suggests that through the slip gap, the geometric differences between the alternative models are near the lower limit for effects on fault slip and the local stress field at the locations of the analyzed events. The 1km edge length of the elements into which faults are discretized may control this scale.

Integrating geological and geophysical data to constrain structural models refines the 3D geometry of major faults along the southern-central Landers rupture, which is critical to understanding the earthquake's multi-fault nature. This is of particular importance because the

surface rupture at Landers is quite complex, particularly in the areas focused on here, and because the fault structure at depth may not be everywhere consistent with the fault traces mapped at the surface. The results have implications for seismic hazard analyses, as further exploration of multi-fault ruptures and fault step-overs would be poorly served by a vertical, continuous fault through the region north of the JVF-HVF step-over, as incorporated into the CFM. Better constraint on the 3D fault structure near fault step-overs is the first step toward a more complete physical representation.

References

Anderson, E. M. (1942). *The Dynamics of Faulting and Dyke Formation with Applications to Britain,* Oliver and Boyd, Edinburgh.

Bryant, W. A. (1992, 1994). Surface rupture along the Johnson Valley, Homestead Valley, and related faults associated with the M7.5 28 June 1992 Landers Earthquake, & Surface fault rupture along the Homestead Valley, Emerson, and related faults associated with the M7.3 28 June 1992 Landers Earthquake, *Div. of Mines & Geology Fault Evaluation Report 234, 239,* CA Dept of Conservation, Sacramento.

Bryant, W. A. (2004). Surface rupture associated with the June 28, 1992, Mw 7.3 Landers earthquake, Iron Ridge, Fry Mountain, and Camp Rock Mine 7.5 minute quadrangles, San Bernardino, CA, *CA Geological Survey unpublished digital mapping for the Pacific Earthquake Engineering Research Center*, Sacramento.

California Geological Survey (2002). GIS files of official maps of Alquist-Priolo earthquake fault zones, southern region, *CA Geological Survey CD 2001-25*, Sacramento.

Comninou, M. A. and J. Dunders (1975). Angular dislocation in a half space, *J. Elasticity* **5** 203-216.

Hardebeck, J. L. and P. M. Shearer (2002). A new method for determining first-motion focal mechanisms, *Bull. Seismo. Soc. Am.* **92** 2264-2276.

Harris, R. A. (2004). Numerical simulations of large earthquakes: Dynamic rupture propagation on heterogeneous faults, *Pure and Applied Geophysics* **161** 2171-2181.

Maerten, F., P. Resor, D. D. Pollard and L. Maerten (2005). Inverting for slip on three-dimensional fault surfaces using angular dislocations, *Bull. Seismo. Soc. Am.* **95** 1654-1665.

Plesch, A., J. H. Shaw, C. Benson, W. A. Bryant, S. Carena, M. Cooke, J. Dolan, G. Fuis, E. Gath, L. Grant, E. Hauksson, T. H. Jordan, M. Kamerling, M. Legg, S. Lindvall, H. Magistrale, C. Nicholson, N. Niemi, M. Oskin, S. Perry, G. Planansky, T. Rockwell, P. Shearer, C. Sorlien, M. P. Süss, J. Suppe, J. Treiman, and R. Yeats (2007). Community fault model (CFM) for southern California, *Bull. Seismo. Soc. Am.* **97** 1793–1802.

Pollard, D. D. and R. C. Fletcher (2005). *Fundamentals of Structural Geology and Geomechanics,* Cambridge University Press, New York.

Spotila, J. A. and K. Sieh (1995). Geologic investigations of a slip gap in the surficial ruptures of the 1992 Landers earthquake, Southern California, *J. Geophys. Res.*, 543-559.

Thomas, A. L. (1993). Poly3D: a three-dimensional, polygonal element, displacement discontinuity boundary element computer program with applications to fractures, faults, and cavities in the Earth's crust, *Master's Thesis*, Stanford University, Stanford, CA.

Zanzerkia, E. (2003). Towards an understanding of seismic triggering through precise earthquake locations, *PhD Thesis*, Stanford University, Stanford, CA.

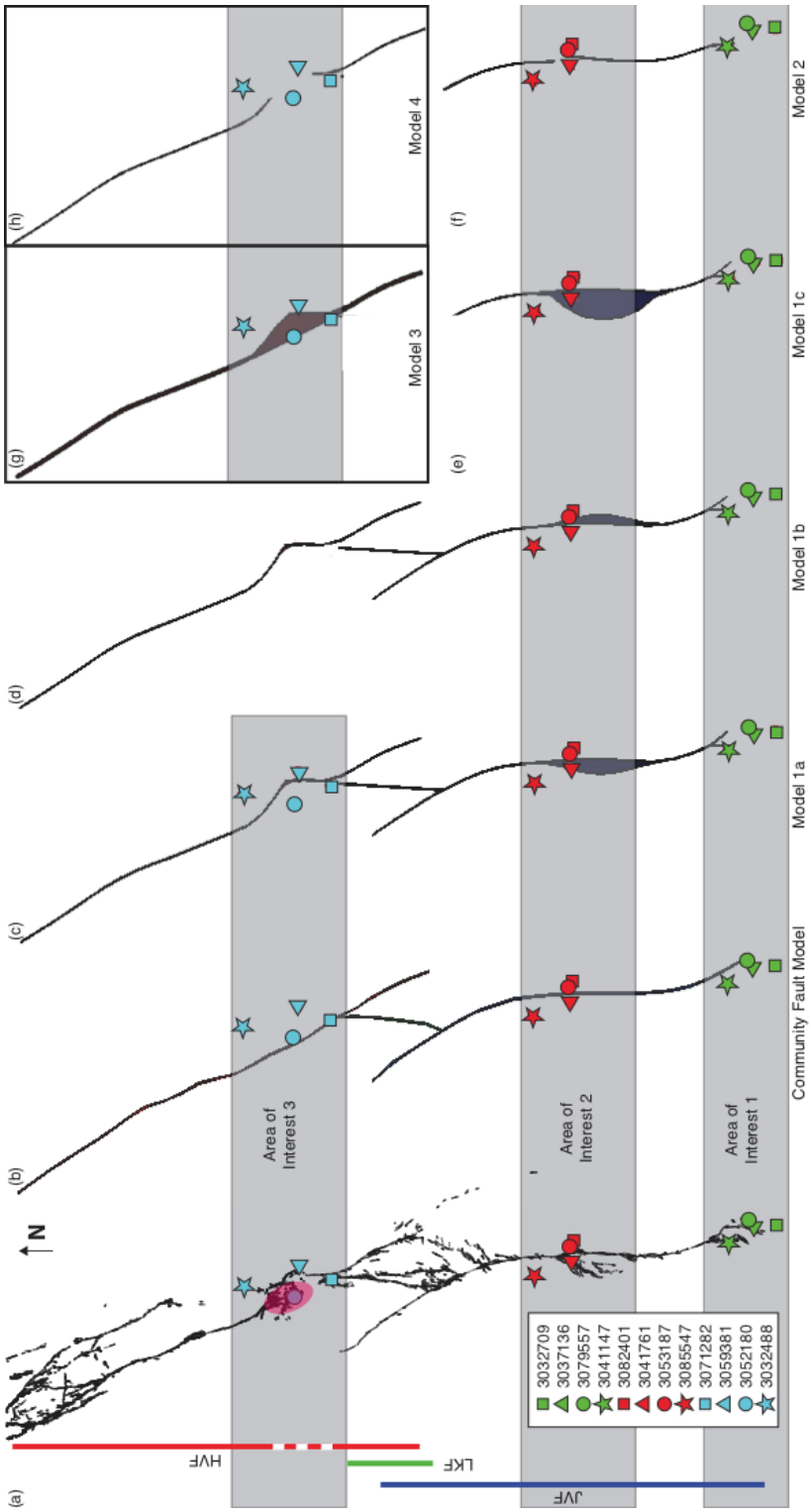

Figure 1: (a) Surface rupture and fault extents shown with color bars, with analyzed aftershocks indicated by icons. Ellipse near slip gap indicates approximate location of the quartz monzonite outcrop. Respectively, (b) through (h) show the geometry of the Community Fault Model (CFM), M1a, M1b, M1c, M2, M3 and M4. Shading indicates which models are compared in each area of interest. Note that M1c and M2 have HVF geometries as in M1a and that M3 and M4 have JVF geometries as in M1a.

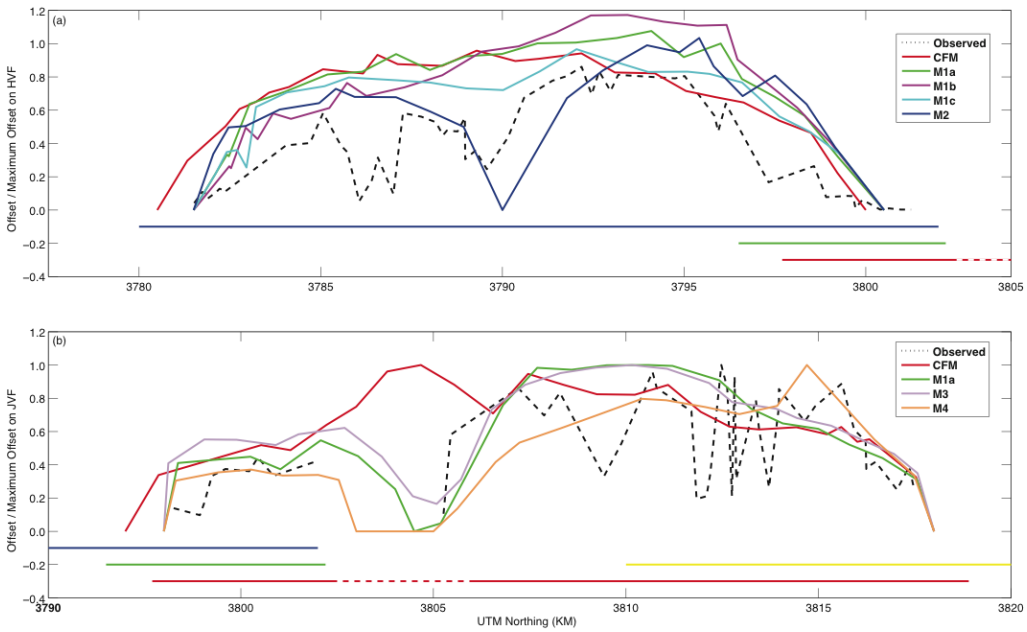

Figure 2: Normalized slip distributions along the (a) JVF and (b) HVF for the CFM and alternative models, with observed values shown in black. Horizontal bars below the slip distributions show the extents of faults, with colors as in Figure 1.

Area	Event ID	mod	fit	S1	D1	R1	U1	diff FP1	diff R1	S2	D2	R2	U2	diff FP2	diff R2
1	3032709	Obs		360	43	250	30			207	50	288	33		
		CFM		163	90	180		49	70	42	90	360		43	72
		M1a		162	90	180		50	70	41	90	360		42	72
		M1b		342	90	180		49	70	221	90	360		42	72
		M1c		342	90	180		49	70	221	90	360		42	72
		M2		162	90	180		50	70	41	90	360		42	72
1	3037136	Obs		352	82	195	34			260	75	352	30		
		CFM		11	59	250		29	55	210	65	289		48	63
		M1a	xx	166	90	185		10	10	45	86	357		40	6
		M1b	x	166	90	183		10	12	45	87	358		38	6
		M1c	x	165	90	184		11	11	44	86	358		40	6
		M2	x	164	87	187		14	8	42	86	354		42	2
1	3079557	Obs		339	87	191	32			248	79	357	31		
		CFM		197	71	225		44	34	59	66	317		36	40
		M1a	xx	164	87	187		8	4	43	85	354		30	3
		M1b	xx	164	88	185		7	6	43	87	356		29	1
		M1c	xx	164	88	186		7	5	42	86	355		30	2
		M2	xx	160	85	187		8	4	39	86	352		33	4
1	3041147	Obs		24	79	201	35			290	69	348	35		
		CFM		347	79	199		37	2	222	80	341		66	7
		M1a		25	61	265		19	64	210	61	275		71	74
		M1b		342	88	183		43	18	221	89	357		70	9
		M1c		18	60	269		20	68	198	61	271		81	78
		M2		188	60	270		43	69	8	61	270		71	78
2	3082401	Obs		123	73	162	27			218	73	18	29		
		CFM		162	73	210		37	48	32	75	329		33	49

		M1a		162	77	203		37	41	36	78	337		29	41
		M1b		158	78	199		34	37	34	80	340		27	38
		M1c	xx	161	84	190		39	28	39	84	350		23	28
		M2		162	82	194		39	32	40	82	346		25	32
2	3041761	Obs		337	39	59	34			195	57	113	33		
		CFM		348	68	224		31	165	209	68	316		17	157
		M1a		215	73	328		85	91	346	73	213		57	100
		M1b		207	67	308		86	111	351	65	231		62	118
		M1c		38	86	351		69	68	160	84	188		42	75
		M2		227	84	347		82	72	349	82	192		47	80
2	3053187	Obs		336	78	186	33			245	84	348	29		
		CFM	x	160	84	190		18	4	38	85	350		29	2
		M1a	x	162	84	190		19	4	40	85	349		27	1
		M1b	x	159	84	191		18	5	37	84	349		30	1
		M1c	xx	342	84	192		9	6	220	83	349		24	1
		M2	x	166	80	198		24	12	42	80	342		28	6
2	3085547	Obs		350	75	196	33			256	75	344	33		
		CFM	xx	350	68	218		7	22	215	73	320		39	24
		M1a	x	352	67	221		8	25	214	71	317		40	28
		M1b	x	351	66	222		9	26	214	72	316		40	28
		M1c	x	353	67	224		8	28	215	69	315		40	29
		M2		4	62	241		19	45	212	65	299		42	46
3	3071282	Obs		173	76	203	34			77	68	345	32		
		CFM	x	157	88	184		20	19	36	88	356		45	12
		M1a	xx	346	88	186		18	17	225	86	355		41	10
		M3	x	348	84	185		21	18	226	89	352		38	8
		M4	x	164	90	183		17	20	223	87	358		42	14
3	3059381	Obs		10	86	181	34			280	89	356	35		
		CFM	xx	166	72	204		32	23	39	80	332		62	24
		M1a		178	64	231		32	50	34	68	308		68	48
		M3		181	58	247		37	66	22	67	291		79	65
		M4		179	63	236		33	55	31	67	303		71	53
3	3052180	Obs		5	71	201	34			268	70	340	32		
		CFM		163	76	204		39	3	37	78	335		60	5
		M1a	x	345	88	179		26	22	44	88	1		48	21
		M3	xx	346	86	179		24	22	45	87	3		48	23
		M4	x	343	89	180		28	21	42	89	1		49	21
3	3032488	Obs		134	77	189	26			42	81	347	30		
		CFM	x	167	70	209		32	20	37	78	328		6	19
		M1a	x	163	83	183		29	6	222	89	353		10	6
		M3	xx	164	80	185		30	4	223	89	349		10	2
		M4	x	163	82	183		29	6	222	89	352		10	5

Table 1: Entries in the ‘Area’ column refer to the area of interest in which the aftershock is located. The identifying numbers of each aftershock analyzed are listed in the ‘Event ID’ column. Rows with focal mechanism information are indicated by the abbreviation Obs in the model column, labeled ‘mod’. x in the ‘fit’ column indicates that the model produces a good fit failure plane, while xx indicates the models producing the best-fit failure planes. Marks may refer to one or both failure plans in the row. ‘S’, ‘D’, and ‘R’ are the strike, dip and rake of the fault and model failure planes. The fault plane uncertainties for each aftershock plane are indicated in the ‘U1’ and ‘U2’ columns. ‘diffFP’ and ‘diffR’ are explained in the text.

Area	Event ID	fit	S1	D1	R1	U1	diff FP1	diff R1	S2	D2	R2	U2	diff FP2	diff R2
1	3032709		360	43	250	30			207	50	288	33		
			167	88	183		50	67	46	88	357		45	69
	3037136		352	82	195	34			260	75	352	30		
		x	350	87	178		6	17	49	87	1		36	10
	3079557		339	87	191	32			248	79	357	31		
		x	164	86	188		8	3	42	85	352		31	5
	3041147		24	79	201	35			290	69	348	35		
		o	344	88	183		41	18	223	89	356		68	8
2	3082401		123	73	162	27			218	73	18	29		
		x	340	89	185		41	23	219	86	356		13	22
	3041761		337	39	59	34			195	57	113	33		
			43	89	356		75	63	164	87	182		41	70
	3053187		336	78	186	33			245	84	348	29		
		x	344	84	191		9	5	221	84	349		23	1
	3085547		350	75	196	33			256	75	344	33		
			358	66	233		12	37	212	66	307		42	37
4	3071282		173	76	203	34			77	68	345	32		
		x	348	85	183		20	20	227	90	354		37	10
	3059381		10	86	181	34			280	89	356	35		
		o	169	68	219		33	38	34	72	320		67	36
	3052180		5	71	201	34			268	70	340	32		
		x	340	88	193		30	8	218	80	351		49	11
	3032488		134	77	189	26			42	81	347	30		
		x	165	78	185		30	4	223	88	347		10	1

Table 2: Columns are as in Table 1, though the ‘mod’ column is not included. x marks in the ‘fit’ column indicate that the model produces a good fit failure plane, while o marks indicate that the preferred model produces a failure plane that is an improvement over the original failure plane produced at that location, though remains outside of the fault plane uncertainty.

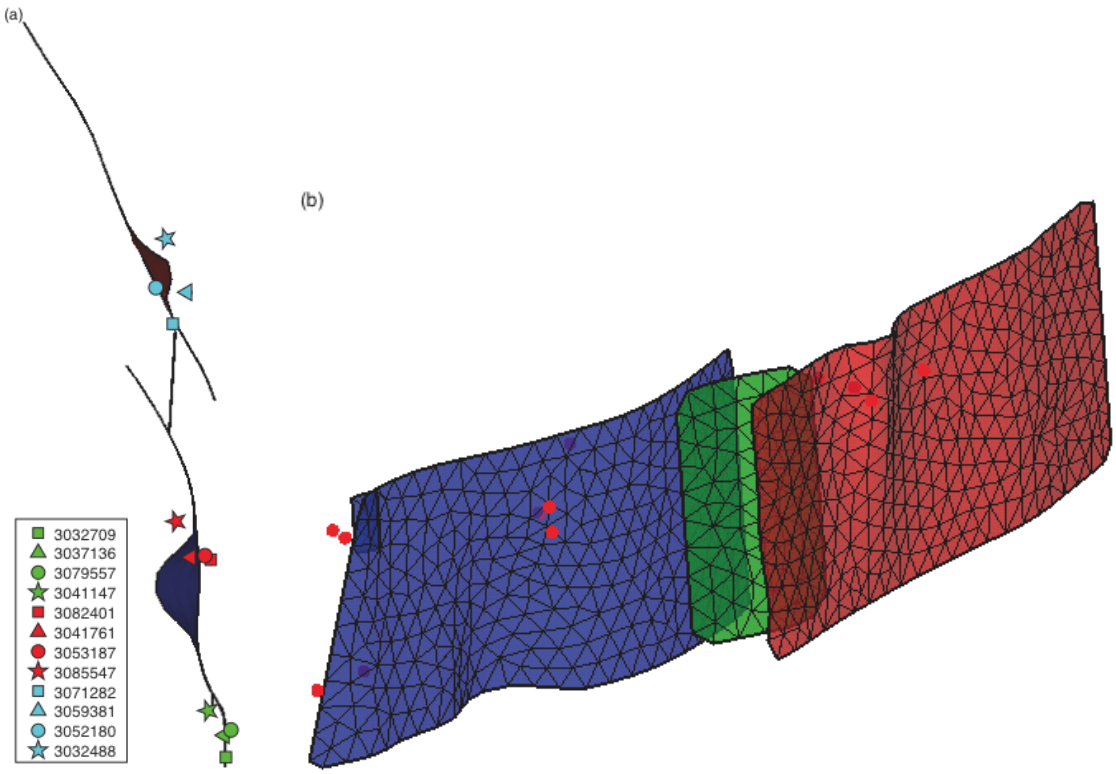

Figure 3: Preferred model geometry in (a) map view with icons show the locations of the analyzed aftershocks, and (b) oblique view, looking northwest. Vertical bars indicate fault extents.

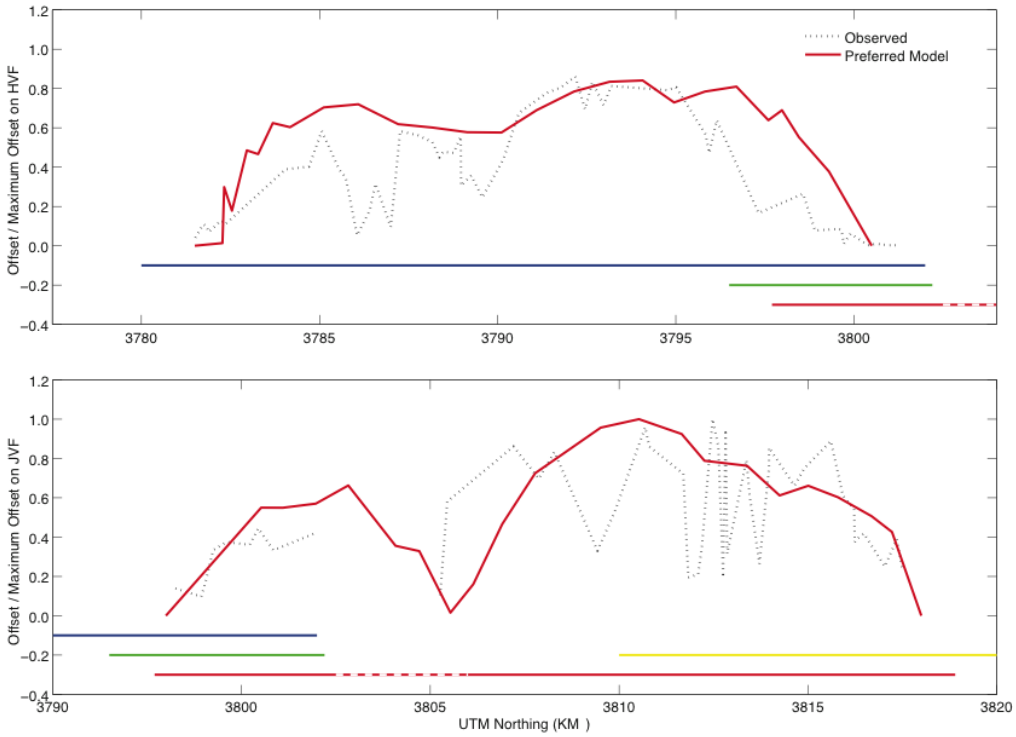

Figure 4: Normalized preferred model slip distributions along the (a) JVF and (b) HVF. Horizontal bars below the slip distributions show the extents of faults, as in Figures 1 and 2.